nature energy

ARTICLES

https://doi.org/10.1038/s41560-021-00967-7

Check for updates

Efficient electrosynthesis of *n*-propanol from carbon monoxide using a Ag–Ru–Cu catalyst

Xue Wang[1,6], Pengfei Ou[1,6], Adnan Ozden[2], Sung-Fu Hung[3], Jason Tam[4], Christine M. Gabardo[2], Jane Y. Howe[4], Jared Sisler[1], Koen Bertens[1], F. Pelayo García de Arquer[1,5], Rui Kai Miao[2], Colin P. O'Brien[2], Ziyun Wang[1], Jehad Abed[1], Armin Sedighian Rasouli[1], Mengjia Sun[1], Alexander H. Ip[1], David Sinton[2] and Edward H. Sargent[1]✉

The high-energy-density C_3 fuel *n*-propanol is desired from CO_2/CO electroreduction, as evidenced by propanol's high market price per tonne (approximately US$ 1,400–1,600). However, CO electroreduction to *n*-propanol has shown low selectivity, limited production rates and poor stability. Here we report catalysts, identified using computational screening, that simultaneously facilitate multiple carbon–carbon coupling, stabilize C_2 intermediates and promote CO adsorption, all leading to improved *n*-propanol electrosynthesis. Experimentally we construct the predicted optimal electrocatalyst based on silver–ruthenium co-doped copper. We achieve, at 300 mA cm^{-2}, a high *n*-propanol Faradaic efficiency of 36% ± 3%, a C_{2+} Faradaic efficiency of 93% and single-pass CO conversion of 85%. The system exhibits 100 h stable *n*-propanol electrosynthesis. Technoeconomic analysis based on the performance of the pilot system projects profitability.

The electrochemical reduction reaction of carbon dioxide (CO_2RR) to valuable fuels and chemical feedstocks offers a promising route to store intermittent renewable electricity[1–5]. However, present-day CO_2RR studies have been performed predominantly in alkaline/neutral electrolytes with a local pH >7 at the catalyst surface during the reaction, leading to the loss of CO_2 through bicarbonate/carbonate formation and added cost for CO_2 regeneration[6]. The electrochemical reduction reaction of carbon monoxide (CORR) following the CO_2 reduction to CO, a two-step cascade process, overcomes this problem[6–8]. Owing to advances in solid oxide electrolysis cell technology, a CO feedstock can now be produced from CO_2 at low cost with an energy efficiency of 90% at ~200 mA cm^{-2}, furthering applications of CORR[9–11].

Among reported C_1–C_3 products in CORR, the C_3 alcohol *n*-propanol is particularly desirable in light of its high energy density and high octane number. It is suitable as an engine fuel, as a solvent and as a feedstock for *n*-propyl acetate[12,13]. Today, *n*-propanol is mainly manufactured via the hydroformylation of ethylene with CO and H_2 to form propionaldehyde, followed by the hydrogenation of propionaldehyde under high pressure and temperature[12]. This complex manufacturing process increases cost and thus limits the overall size of the *n*-propanol market[13]; yet, in light of its higher energy density, *n*-propanol could take the place of ethanol as a transportation fuel additive for which the market would grow if *n*-propanol could be efficiently produced. Hence, it is attractive to explore whether *n*-propanol could be generated efficiently through electrolysis using renewable electricity[13,14].

The present-day performance of *n*-propanol electrosynthesis—including selectivity, production rate and stability—remains low and far below the requirements of practical applications. Technoeconomic analysis (TEA) has shown that reaction rates must exceed at least 100 mA cm^{-2} for profitable CORR systems[7]. Experimentally, previous CORR/CO_2RR systems with current densities above 100 mA cm^{-2} have shown limited selectivity towards *n*-propanol, with a maximum Faradaic efficiency (FE) of 18% and little information on operando stability (Supplementary Table 1)[6,15–20].

The generation of C_3 in CORR relies on C_1–C_1 coupling and subsequent C_1–C_2 coupling. The key step branching the pathways to C_3 and C_2 products is identified as coupling between C_1 and C_2 intermediates[21,22]. To ensure the production of C_3 at high production rates, C_2 intermediates must be formed and stabilized on the catalyst surface and thus be available to be coupled with adsorbed CO (ref. [16]).

We took the view, therefore, that to promote C_3 selectivity at high production rates, a good catalyst would simultaneously facilitate both the C_1–C_1 and the C_1–C_2 coupling steps, stabilize C_2 intermediates and promote CO adsorption. In this Article, we present a catalyst design—silver–ruthenium co-doped copper (Ag–Ru–Cu) catalysts—with high selectivity, production rate and stability for *n*-propanol electrosynthesis. We report a *n*-propanol FE of 37% ± 3% at a production rate of 111 ± 9 mA cm^{-2} in CORR, a more than two times improvement compared with the value reported at total current density above 100 mA cm^{-2} (refs. [6,15–20]) and 100 h stable *n*-propanol electrosynthesis at 300 mA cm^{-2}. We further demonstrate scaling of *n*-propanol electrosynthesis on Ag–Ru–Cu catalysts to 15 cm^2, which delivers an *n*-propanol FE of 36% ± 3% and a C_{2+} FE of 93% with a high single-pass CO conversion of 85%.

Theoretical calculations

We began by using density functional theory (DFT) calculations to screen catalyst systems considering their propensity to catalyse the C_1–C_1 and C_1–C_2 coupling. Ag-doped Cu (Ag–Cu) is an experimentally reported bimetallic catalyst that favours the selectivity to

[1]Department of Electrical and Computer Engineering, University of Toronto, Toronto, Ontario, Canada. [2]Department of Mechanical and Industrial Engineering, University of Toronto, Toronto, Ontario, Canada. [3]Department of Applied Chemistry, National Yang Ming Chiao Tung University, Hsinchu, Taiwan. [4]Department of Materials Science and Engineering, University of Toronto, Toronto, Ontario, Canada. [5]Present address: ICFO – Institut de Ciències Fotòniques, Barcelona Institute of Science and Technology, Barcelona, Spain. [6]These authors contributed equally: Xue Wang, Pengfei Ou. ✉e-mail: ted.sargent@utoronto.ca

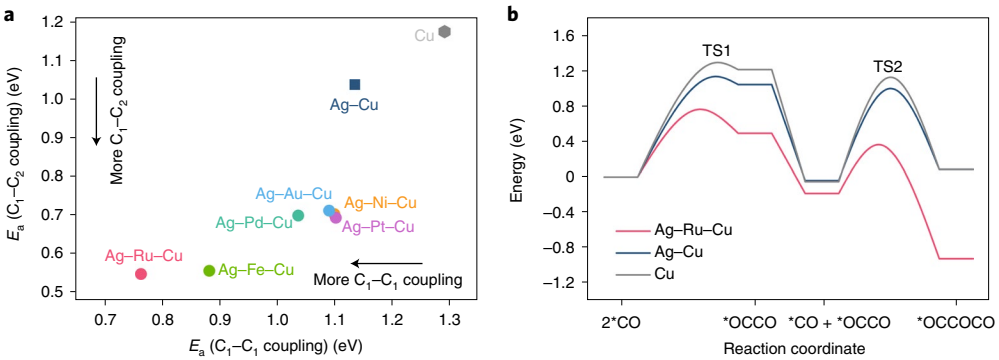

Fig. 1 | DFT calculations on C_1–C_1 and C_1–C_2 coupling. a, The calculated activation energy (E_a) for C_1–C_1 and C_1–C_2 coupling on screened Ag-X-Cu, where X is Au, Pd, Pt, Ni, Fe and Ru. X is categorized into three different groups according to the CO adsorption energies with reference to Cu: (1) weak, Au; (2) intermediate, Pd, Pt and Ni; (3) strong, Fe and Ru. The E_a (C_1–C_1 coupling) and E_a (C_1–C_2 coupling) on Ag–Cu and Cu catalyst systems are also calculated for comparison. **b**, Reaction coordinate diagram for C_1–C_1 and C_1–C_2 coupling on Ag–Ru–Cu, Ag–Cu and Cu catalyst systems. TS1 and TS2 denote the transition state of C_1–C_1 and C_1–C_2 coupling, that is, *CO–*CO and *CO–*OCCO, respectively.

n-propanol compared with Cu (ref. [23]). We therefore considered several Ag–X co-doped Cu (Ag–X–Cu, where X represents an additional metal) catalyst systems for computational screening (Fig. 1a, Supplementary Figs. 1–9 and Supplementary Tables 2 and 3). On the basis of previous studies[16,17,21,23–28], we calculated the activation energies of the *CO dimerization (*CO + *CO → *OCCO) and the coupling between *CO and *OCCO intermediates (*CO + *OCCO → *OCCOCO) on different Ag–X–Cu catalyst systems and then applied them as predictors for the activities of C_1–C_1 and C_1–C_2 coupling, respectively. Of the catalyst systems screened, Ag–Ru–Cu requires the lowest activation energies for both C_1–C_1 and C_1–C_2 coupling (Fig. 1a).

We further compared the adsorption energies of *CO and *OCCO, the key reaction intermediates associated with the C_1–C_1 and C_1–C_2 coupling[16,17,23], on Ag–Ru–Cu versus those on Ag–Cu and Cu (Fig. 1b and Supplementary Fig. 10). Relative to Ag–Cu and Cu, the higher average *CO adsorption energy on Ag–Ru–Cu indicates that CO molecules are more readily adsorbed on Ag–Ru–Cu. Specifically, the co-doping of Ag and Ru in Cu induces CO adsorption near the C_1–C_1 and C_1–C_2 coupling sites and thus results in higher *CO coverage on the surface compared with Ag–Cu and Cu, which may promote multiple C–C coupling (Supplementary Tables 2 and 4). Additionally, the adsorption energy of the key C_2 intermediate for C_1–C_2 coupling on Ag–Ru–Cu is higher than that on Ag–Cu and Cu; this may reduce the desorption of C_2 intermediates from the Ag–Ru–Cu surface and the subsequent formation of C_2 products, thus increasing the residence of C_2 intermediates necessary for C_3 generation. These calculations, taken together, suggest that Ag–Ru–Cu has the potential to improve C_3 selectivity at high production rates.

Catalyst preparation and characterization

We sought to realize Ag–Ru–Cu catalysts experimentally. We first spray coated a layer of commercial Cu nanoparticles onto a gas-diffusion layer (Supplementary Fig. 11a). Then, we prepared the Ag–Ru–Cu catalyst (Fig. 2a,b and Supplementary Fig. 11b) via a two-step galvanic replacement between Cu and $RuCl_3$ and then between Cu and $AgNO_3$—driven by the difference in the reduction potentials of Ru versus Cu and Ag versus Cu (refs. [29–31]), respectively. We observed no appreciable difference in morphology for Ag–Ru–Cu versus the pristine Cu based on scanning electron microscopy (SEM; Supplementary Fig. 11). Energy-dispersive X-ray (EDX) spectroscopy elemental mapping reveals that Ag, Ru and Cu elements are evenly distributed in the Ag–Ru–Cu nanoparticles (Fig. 2c). In the powder X-ray diffraction (XRD) patterns of the Cu and Ag–Ru–Cu electrodes, we observe peaks of Cu_2O ascribed to the partial oxidation of Cu nanoparticles in air during electrode preparation (Supplementary Fig. 12). High-resolution X-ray photoelectron spectroscopy (XPS) further confirms the existence of Cu, Ag and Ru in the nanoparticles (Fig. 2d–f and Supplementary Fig. 13). The atomic percentages of Ag and Ru in the electrode near the surface are approximately 4% and 1%, respectively, as determined using XPS.

Investigation on electroreduction of CO

The CORR performance was evaluated in a membrane electrode assembly (MEA) electrolyser with both cathode and anode electrodes having a 5 cm^2 active geometric area ($A = 5$ cm^2) (Supplementary Figs. 14 and 15). Figure 3a displays the FEs of C_{2+} products (ethylene, ethanol, acetate and *n*-propanol) on Ag–Ru–Cu and Cu electrodes during CORR in the current density range of 200–600 mA cm^{-2}. Ag–Ru–Cu electrodes delivered higher selectivities to total C_{2+} products and to *n*-propanol, relative to Cu electrodes (Supplementary Table 5 and Supplementary Fig. 16), consistent with DFT predictions (Fig. 1). In the regime of 300–600 mA cm^{-2}, the total FEs for C_{2+} products reach 90%, and the highest C_{2+} partial current density reaches 540 mA cm^{-2} for the Ag–Ru–Cu electrodes (Fig. 3b). Specifically, under a current density of 300 mA cm^{-2}, we achieve an *n*-propanol FE of 37% ± 3% on Ag–Ru–Cu electrodes—1.8 times higher than that on Cu electrodes—at a production rate of 111 ± 9 mA cm^{-2} associated with a full-cell potential of −2.75 ± 0.01 V. This is a directly measured full-cell voltage; that is, it does not include any correction from ohmic losses.

To explore further the effect of co-doping Ag and Ru into Cu on CORR performance, we prepared Ag–Cu electrodes and measured their CORR performance for comparison. The Ag–Cu electrodes were prepared via the same galvanic-replacement approach, and the atomic percentage of Ag doping in Cu on the electrode surface was also approximately 4%, as determined by XPS (Supplementary Figs. 17–19). At the same current densities, the total FEs towards C_{2+} products on the Ag–Cu electrodes are higher than those on Cu electrodes but lower than those on Ag–Ru–Cu electrodes (Supplementary Table 5). This indicates that the Ag doping in Cu favours C_1–C_1 coupling for C_{2+} products relative to Cu, and the co-doping of Ag and Ru further enhances the C_{2+} selectivity. The *n*-propanol FEs on different electrodes follow the sequence Ag–Ru–Cu > Ag–Cu > Cu (Fig. 3c), suggesting that co-doping of Ag and Ru in Cu also promotes the step of C_1–C_2 coupling versus Ag–Cu and Cu, in agreement with calculations (Fig. 1). At 500 mA cm^{-2}, the highest partial *n*-propanol current density on the Ag–Ru–Cu

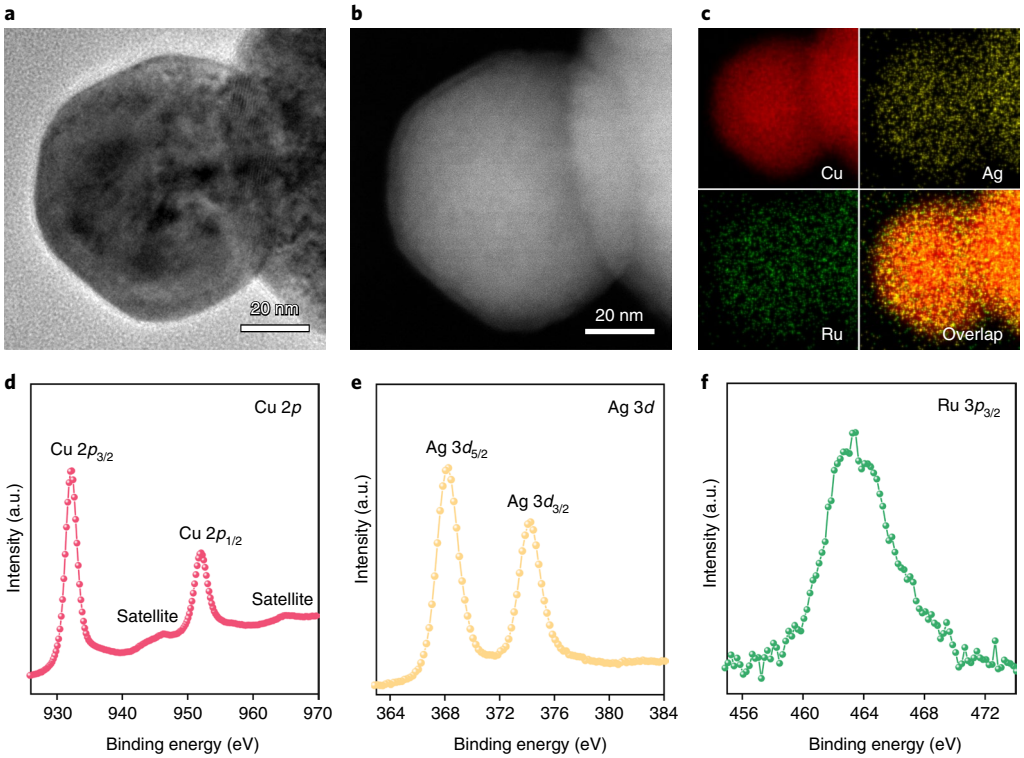

Fig. 2 | Structural and compositional analyses of the Ag–Ru–Cu catalysts. a–c, Bright-field scanning transmission electron microscopy image (**a**) and high-angle annular dark-field scanning transmission electron microscopy image (**b**) of the Ag–Ru–Cu catalyst and the corresponding EDX spectroscopy elemental mapping of Cu, Ag and Ru (**c**). Both SEM and TEM measurements were repeated at least twice independently, and similar results were obtained. **d–f**, High-resolution XPS spectra of Cu 2*p* (**d**), Ag 3*d* (**e**) and Ru $3p_{3/2}$ (**f**) for the Ag–Ru–Cu catalysts.

electrodes is $153 \pm 12\,mA\,cm^{-2}$, representing 1.3 times and 1.5 times improvement relative to the Ag–Cu and Cu electrodes, respectively (Fig. 3c).

To evaluate the selectivity towards *n*-propanol versus C_2 products in CORR, we compare the ratios of *n*-propanol FE to total C_2 FE ($\frac{FE_{n\text{-PrOH}}}{FE_{C_2}}$) on different electrodes. Relative to the Ag–Cu and Cu electrodes, the Ag–Ru–Cu electrodes display higher $\frac{FE_{n\text{-PrOH}}}{FE_{C_2}}$ (Fig. 3d), further suggesting that the co-doping of Ag and Ru in Cu promotes the coupling reaction between C_1 and the C_2 intermediates.

As controls, we also prepared Ag–Au–Cu and Ag–Pd–Cu electrodes (Supplementary Figs. 20–23) and measured their CORR performance (Supplementary Figs. 24 and 25). By comparing the *n*-propanol FEs under the same current densities among different electrodes, we find that Ag–Au–Cu and Ag–Pd–Cu electrodes exhibit lower *n*-propanol selectivity than Ag–Ru–Cu electrodes but higher *n*-propanol selectivity relative to Ag–Cu and Cu electrodes, in agreement with calculations.

We evaluated the CORR stability on the Ag–Ru–Cu electrode at $300\,mA\,cm^{-2}$ in the MEA electrolyser (Fig. 3e and Supplementary Fig. 26). The system maintained a stable full-cell potential of -2.64 ± 0.07 V during the CORR measurement. Throughout 100 h of continuous operation, an *n*-propanol FE above 32% was maintained using the Ag–Ru–Cu electrode. Transmission electron microscopy (TEM), EDX and XPS analyses on post-reaction catalysts reveal that the Ag–Ru–Cu catalyst retains its structure following extended operation (Supplementary Figs. 27 and 28).

To investigate the chemical state of Cu in different catalysts during CORR, we carried out in situ X-ray absorption spectroscopy (XAS) studies at the Cu K-edge. The Cu K-edge X-ray absorption near-edge structure spectra reveal that under a current density of $300\,mA\,cm^{-2}$, the average valence states of Cu in Ag–Ru–Cu, Ag–Cu and Cu are all zero during CORR (Supplementary Fig. 29). We conclude that product selectivities on Ag–Ru–Cu, Ag–Cu and Cu catalysts in CORR are all derived from metallic Cu (refs. [15,32–34]).

To gain insights into the C–C coupling mechanism in different catalysts, we also performed in situ Raman spectroscopy measurements during CORR under different potentials (Fig. 4a and Supplementary Fig. 30). The bands in the range of 1,900–2,150 cm^{-1} arise from the C≡O stretching of the adsorbed CO on metal sites[35–37], wherein the regions below and above 2,000 cm^{-1} are attributed to the bridge-bound CO (CO_{bridge})—which is not an on-pathway intermediate in CORR—and the atop-bound CO (CO_{atop}), respectively[35–37]. Relative to Cu, the C≡O stretching bands on Ag–Ru–Cu and Ag–Cu are only from CO_{atop} on the surface, indicating that the adsorbed CO on Ag–Ru–Cu and Ag–Cu is in a more favourable configuration for further reaction to C_{2+} products compared with Cu (ref. [37]).

In the Raman spectra, the bands located at ~283 cm^{-1} and ~363 cm^{-1} are associated with frustrated rotation of *CO on Cu and Cu–CO stretching, respectively. Under the same applied potentials, we observe a blueshift of the Cu–CO stretching band on Ag–Ru–Cu relative to Ag–Cu and Cu (Fig. 4a). The blueshift of the Cu–CO stretching band indicates a stronger Cu–CO bond on the Ag–Ru–Cu surface compared with the Ag–Cu and Cu surfaces[38], which might favour the C–C coupling step and subsequent generation of C_{2+} products[5,39]. As controls, we also acquired in situ Raman spectra with the Ar-saturated KOH electrolyte to confirm that the peaks in the regions marked orange, blue and yellow arise from the conditions of CORR (Fig. 4a and Supplementary Fig. 31).

We investigated the extent to which *n*-propanol electrosynthesis can be scaled, seeking to increase the active area to 15 cm^2 ($A = 15$ cm^2; Fig. 4b, Supplementary Figs. 32 and 33 and Supplementary Table 6). We achieved, at a current density of $300\,mA\,cm^{-2}$,

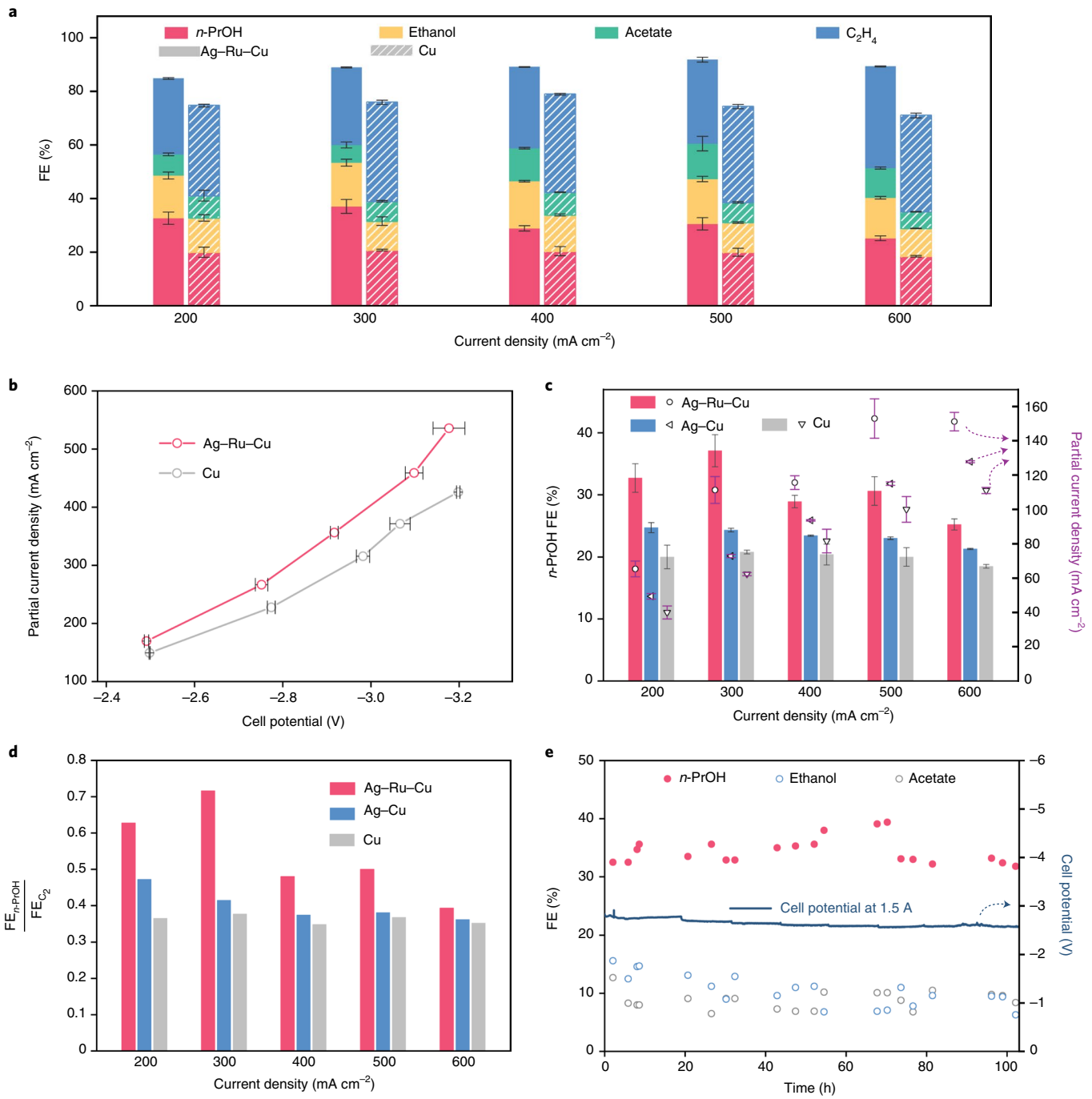

Fig. 3 | CORR performance of different cathode electrodes. a, C_{2+} product distribution under different current densities for Ag–Ru–Cu and Cu electrodes. Error bars represent the standard deviation of three independent samples. Data are presented as mean values ± standard deviation. **b**, Partial current densities of C_{2+} products for Ag–Ru–Cu and Cu electrodes under different potentials. Error bars represent the standard deviation of potentials (>660 data points collected in one experiment) during the constant current electrolysis. Data are presented as mean values ± standard deviation. **c**, *n*-Propanol (*n*-PrOH) FEs and partial *n*-propanol current densities on different electrodes at various current densities. Error bars represent the standard deviation of three independent samples. Data are presented as mean values ± standard deviation. **d**, Comparison of $\frac{FE_{n\text{-PrOH}}}{FE_{C_2}}$ ratios on different electrodes at various current densities. **e**, Liquid product distribution and cell voltage during 102 h operation of CORR at a constant current of 1.5 A. CO feed rate in all these experiments is 47.0 ml min^{-1}.

n-propanol FE of 36% ± 3% and a C_{2+} FE of 93% at a full-cell potential of −2.60 ± 0.02 V (again, without ohmic loss correction); this corresponds to a full-cell energy efficiency of 37% for all C_{2+} products. To reduce the energy penalty of unreacted CO and gas product separation after reaction, we pursued a high single-pass CO conversion (SPCC) in the system. We lowered the CO feed rate and observed that Ag–Ru–Cu catalysts could retain similar product selectivities at a low CO feed rate; as a result, we achieved a SPCC as high as 85% for C_{2+} products.

To assess the economic potential of the *n*-propanol electrosynthesis powered by renewable electricity, we performed a TEA for the process, where *n*-propanol, ethanol, ethylene and H_2 products

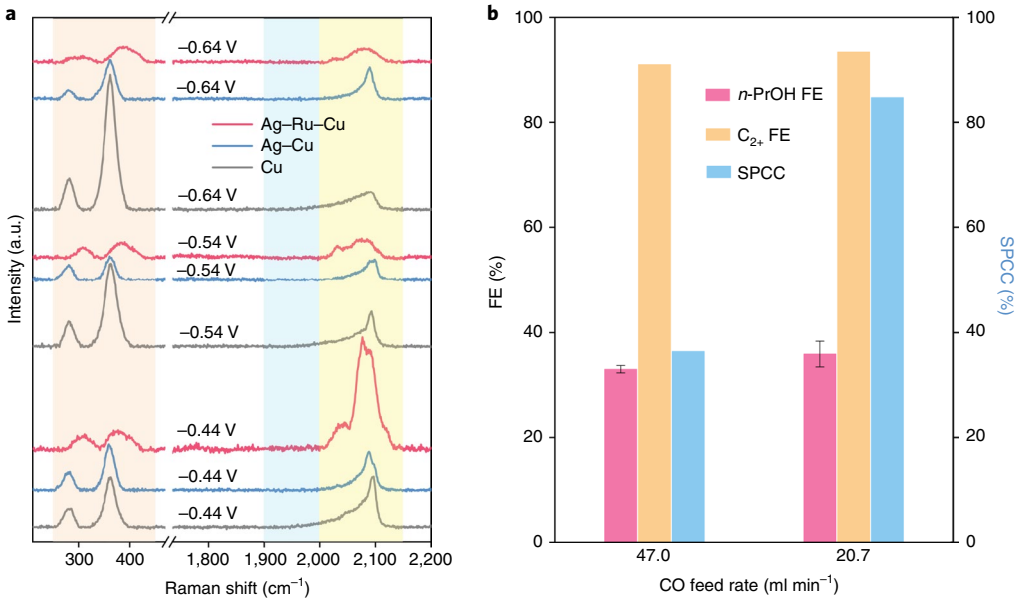

Fig. 4 | In situ characterization and *n*-propanol electrosynthesis in a larger electrolyser. a, In situ Raman spectra of different catalysts under different applied potentials versus RHE using 1 M KOH electrolyte during CORR. The regions of 250–450 cm^{-1}, 1,900–2,000 cm^{-1} and 2,000–2,150 cm^{-1} are marked by orange, blue and yellow, respectively. The Raman shift in the range of 470 cm^{-1} to 1,735 cm^{-1} is marked by the break in the *x* axis. **b**, FEs towards *n*-propanol and C_{2+} products and SPCC with different CO feed rates at the applied current of 4.5 A in the $A = 15\ cm^2$ MEA electrolyser. Error bars represent the standard deviation of three independent samples. Data are presented as mean values ± standard deviation.

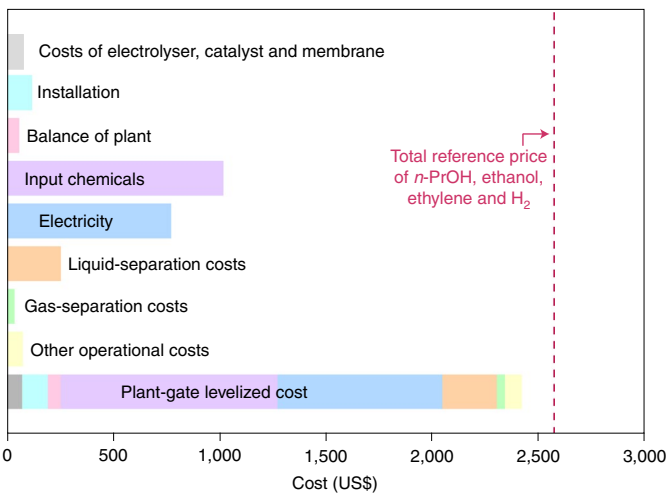

Fig. 5 | Breakdown of the plant-gate levelized cost per tonne of *n*-propanol and the corresponding quantity of ethanol, ethylene and H_2 produced on Ag–Ru–Cu at a current density of 300 mA cm^{-2}. The TEA findings are calculated based on the CORR performance in the $A = 15\ cm^2$ MEA electrolyser with a CO feed rate of 20.7 ml min^{-1}. The total reference price of *n*-propanol, ethanol and H_2 is marked by the red dashed line.

are considered as the products for sale in the calculation (Fig. 5, Supplementary Figs. 34 and 35 and Supplementary Table 7). We accounted for the cost of separation, including the separation of liquid products from one another and gas products from one another; the costs for the electrolyser, catalyst, membrane, installation, balance of plant, input chemicals and electricity; and the other operational costs (such as labour and maintenance; Supplementary Methods). Sensitivity analysis reveals that the plant-gate levelized cost depends most importantly on electricity cost and on electrochemical performance parameters such as *n*-propanol FE, current density, SPCC and full-cell potential (Supplementary Fig. 35, and Supplementary Table 7). Further calculation reveals that with an *n*-propanol FE of 36%, the renewable electricity-powered *n*-propanol electrosynthesis becomes profitable only when the current density is higher than 150 mA cm^{-2} and SPCC is above 15% (Supplementary Fig. 36).

The TEA calculation—based on the CORR performance data at 300 mA cm^{-2} in the $A = 15\ cm^2$ MEA electrolyser—shows that the plant-gate levelized cost for 1 tonne of *n*-propanol, plus the corresponding quantity of ethanol, ethylene and H_2 produced at 300 mA cm^{-2} on Ag–Ru–Cu electrodes, is projected to be less than the sum of their reference prices (Fig. 5). This result suggests that the CORR on the Ag–Ru–Cu electrodes under the above conditions shows promise.

Conclusions

We report Ag–Ru–Cu catalysts that enable *n*-propanol FE of 37% ± 3% at a partial current density of 111 ± 9 mA cm^{-2} during CORR. We also achieve 100 h stable *n*-propanol electrosynthesis at 300 mA cm^{-2}. The performance of Ag–Ru–Cu electrodes outperforms other reported *n*-propanol electrosynthesis in selectivity, current density and operation time. We scale *n*-propanol electrosynthesis to 15 cm^2 MEA, achieving the performance, including *n*-propanol FE of 36% ± 3% and a C_{2+} FE of 93% at the full-cell potential of −2.60 ± 0.02 V, together with an SPCC of 85% and full-cell energy efficiency of 37% for all C_{2+} products. The TEA suggests the CORR-to-*n*-propanol system has a path to become profitable. This work paves a way for the efficient electrosynthesis of C_3 products and the decarbonization of the petrochemical industry.

Methods

Chemicals. Silver nitrate ($AgNO_3$, 99.0%), ruthenium (III) chloride hydrate ($RuCl_3 \cdot xH_2O$) and iridium (III) chloride hydrate ($IrCl_3 \cdot xH_2O$, 99.9%) were purchased from Sigma-Aldrich. Potassium hydroxide (KOH) was received from Caledon Laboratory Chemical. Anion-exchange membrane (Fumasep FAA-3-50) and titanium mesh were received from Fuel Cell Store. Sustainion anion-exchange membrane was purchased from Dioxide Materials. The anion-exchange membranes were activated before use[5]. Copper target (99.999%) was purchased from Kurt J. Lesker.

Polytetrafluoroethylene membrane with an average pore size of 450 nm was received from Beijing Zhongxingweiye Instrument. All chemicals were used as received. The aqueous solutions were prepared using distilled water with a resistivity of 18.2 MΩ cm.

Preparation of electrodes. We first prepared a conductive gas-diffusion layer by sputtering 50-nm-thick Cu (Cu target, sputtering rate ~0.6 Å s^{-1}) on a piece of PTFE membrane using a magnetron sputtering system. Cu nanoparticles (Sigma-Aldrich) were dispersed in a mixture of methanol and Nafion perfluorinated resin solution (5 wt% in a mixture of lower aliphatic alcohols and water; Sigma-Aldrich) under ultrasonication for 30 min to prepare a suspension with a Cu concentration of 9.9 mg ml^{-1}. The suspension was spray coated on the gas-diffusion layer with a Cu nanoparticle loading of 6 mg cm^{-2} to prepare the Cu electrode. For the experiments in the $A = 15\ cm^2$ MEA electrolyser, the Cu electrode was prepared by directly spray coating the suspension on the carbon-based gas-diffusion layer.

To prepare the Ag–Ru–Cu electrode, we first immersed the prepared Cu electrode in a N_2-saturated 5 μmol l^{-1} $RuCl_3$ aqueous solution at 65 °C for 20 min and then immersed the electrode in a N_2-saturated 5 μmol l^{-1} $AgNO_3$ aqueous solution at 65 °C for 2 h. The Ag–Cu electrode, Ag–Au–Cu electrode and Ag–Pd–Cu electrode were prepared using a similar galvanic-replacement approach. For the Ag–Cu electrode, the prepared Cu electrode was immersed in N_2-saturated distilled water at 65 °C for 20 min and then in a N_2-saturated 5 μmol l^{-1} $AgNO_3$ aqueous solution at 65 °C for 2 h. For the Ag–Au–Cu electrode, the prepared Cu electrode was immersed in a N_2-saturated 5 μmol l^{-1} $HAuCl_4$ aqueous solution at 40 °C for 15 min and then in a N_2-saturated 5 μmol l^{-1} $AgNO_3$ aqueous solution at 65 °C for 2 h. For the Ag–Pd–Cu electrode, the prepared Cu electrode was immersed in a N_2-saturated 5 μmol l^{-1} H_2PdCl_4 aqueous solution at 65 °C for 20 min and then in a N_2-saturated 5 μmol l^{-1} $AgNO_3$ aqueous solution at 65 °C for 2 h. The anode catalyst is titanium mesh-supported iridium oxide (IrO_x/Ti mesh) prepared by a previously reported dip coating and thermal decomposition method[40].

Materials characterization. SEM images were taken using a Hitachi FE-SEM SU5000 microscope. High-angle annular dark-field scanning transmission electron microscopy images and the corresponding EDX elemental mapping were taken using a Hitachi HF-3300 microscope at 300 kV. Cathode structure and surface composition characterization were carried out using XRD (MiniFlex600) with Cu-Kα radiation and XPS (model 5600, PerkinElmer) with a monochromatic aluminium X-ray source, respectively.

In situ Raman measurements were performed using a Renishaw inVia Raman Microscope (water immersion objective (×63), 785 nm laser) in a modified flow cell with 1 M KOH aqueous solution as the electrolyte (Supplementary Fig. 30). The different prepared cathode catalysts, Ag/AgCl reference electrode (3 M KCl, BASi) and platinum coil were used as the working electrodes, reference electrode and counter electrode, respectively. CO or Ar was continuously supplied to the gas chamber during the measurement. The potentials (E) in Raman measurement were converted to values versus the reversible hydrogen electrode (RHE) using the equation: $E_{RHE} = E_{Ag/AgCl} + 0.210\ V + 0.0591 \times pH$.

In situ XAS measurements were conducted at BL-17C at the National Synchrotron Radiation Research Center. We measured in situ XAS spectra at 300 mA cm^{-2} during CORR using a flow-cell reactor, a configuration the same as that used in a previous report[15,23]. In the flow-cell reactor, an Ag/AgCl reference electrode (3 M KCl, BASi; reference electrode), Ni foam (1.6 nm thickness, MTI Corporation; anode) and anion-exchange membrane (Fumasep FAB-PK-130, Fuel Cell Store; membrane) were used. 1 M KOH aqueous solution was used as the electrolyte, and CO (Linde, 99.99%) was continuously supplied to the gas chamber during CORR. XAS data were processed using ATHENA and ARTEMIS software included in a standard IFEFFIT package[41].

Electrochemical measurements. Without specification, all the CORR performance was measured in the $A = 5\ cm^2$ MEA electrolyser (SKU: 68732; Dioxide Materials) (Supplementary Figs. 14 and 15). The MEA electrolyser installation procedure is the same as that used in our previous report[5]. For the $A = 15\ cm^2$ MEA electrolyser (Supplementary Fig. 32), the cathode electrode (3.875 cm × 3.875 cm) was positioned on the cathode side and thus the activated Sustainion membrane (6.5 cm × 6.5 cm) and an IrO_x/Ti mesh anode electrode (3.875 cm × 3.875 cm) was put on top of the cathode, successively; all were assembled in the MEA electrolyser.

The MEA electrolyser-based CORR measurement procedure is similar to that used in a previous report[5]. CO gas (Linde, 99.99%) at different feed rates flowed to the humidifier with distilled water continuously and was then supplied to the cathode chamber. Anolyte (1 M KOH aqueous solution) was introduced into the anode chamber and was circulated using a pump (10 ml min^{-1}). Using an electrochemical station (AUT50783) equipped with a current booster (10 A), we evaluated the performance of the cathode electrode in a two-electrode system at different current densities. The long-term operation test was also performed in the MEA electrolyser, and the anion-exchange membrane (Fumasep FAB-PK-130) was used as the membrane. The products from the cathode side went through a simplified cold trap that was used for separating liquid products and gas products. The gas products were tested by gas chromatograph (PerkinElmer Clarus 600). The liquid products were analysed using a NMR spectrometer (Agilent DD2 600 MHz) with dimethylsulfoxide as an internal standard. Liquid product FE was calculated by considering the total amount of the products collected from anode and cathode sides in the same period.

Full-cell energy efficiency calculation. For different products, A (*n*-propanol, ethanol, ethylene and acetate), the full-cell energy efficiency for product A is calculated as follows[5]:

$$EE_{\text{full cell, A}} = \frac{(1.23 + (-E_A^o)) \times FE_A}{-E_{\text{full cell}}}$$

where E_A^o is the thermodynamic potential of CO to product A ($E_{n\text{-PrOH}}^o = 0.20$ V versus RHE; $E_{\text{ethanol}}^o = 0.178$ V versus RHE; $E_{\text{ethylene}}^o = 0.17$ V versus RHE; $E_{\text{acetate}}^o = 0.454$ V versus RHE) calculated based on the standard molar Gibbs energy formation at 298.15 K (refs. [23,42]), FE_A is the measured FE (%) of the product A, and $E_{\text{full-cell}}$ is the full-cell voltage measured in the MEA system without ohmic loss correction.

SPCC calculation. Under the conditions of 298.15 K and 101.3 kPa, SPCC is calculated as follows:

$$\text{Total SPCC} = 60\ (\text{s}) \times \sum \frac{\text{Total current (A)} \times FE_A \times \text{Molar ratio}\left(\frac{CO}{\text{product A}}\right)}{\text{Electrons transferred for every product A molecule} \times \text{Faraday's constant}} \div \frac{\text{CO feed rate}\left(\frac{l}{\text{min}}\right) \times 1\ (\text{min})}{\frac{8.314\ \left(\text{J mol}^{-1}\ \text{K}^{-1}\right) \times 298.15\ (\text{K})}{101{,}300\ (\text{Pa})}}$$

DFT calculations. All ab initio DFT calculations were performed by employing the projector-augmented wave method as implemented in the Vienna Ab initio Simulation Package[43–46]. The generalized gradient approximation in the parametrization of Perdew–Burke–Ernzerhof was implemented to describe the exchange-correlation functional[47]. A plane-wave cut-off of 450 eV and 2 × 4 × 1 gamma-centred *k*-point grids generated by the Monkhorst–Pack scheme were used for all the calculations[48]. A vacuum region of more than 15 Å thickness was included along the perpendicular direction to avoid artificial interactions. The zero damping DFT-D3 method of Grimme was employed to better capture long-range dispersion interactions[49].

The Ag–Cu (111) and Cu (111) structures were constructed based on our previous study[23]. For the screened Ag–X–Cu (X: Au, Pd, Pt, Ni, Fe and Ru) systems, one Cu atom on the top layer of a four layer (6 × 3) Ag–Cu (111) supercell was substituted with Au, Pd, Pt, Ni, Fe and Ru (Supplementary Figs. 1–8). The position of the substituted atom was determined by the structure with the lowest energy in our benchmark calculations (Supplementary Note 1 and Supplementary Fig. 9). The number of adsorbed *CO near the coupling sites was determined using the adsorption energy of *CO on Ag–X–Cu relative to Cu (Supplementary Note 1 and Supplementary Table 2). A monolayer of charged water molecules was included in all initial, transition and final states of C_1–C_1 and C_1–C_2 coupling above the surface to account for the combined field and solvation effects[50]. Geometries of the initial and final states were optimized by a force-based conjugate gradient algorithm with two upper layers together with the water molecules and adsorbates being allowed to relax, while the atoms in the two lower layers were fixed. The transition states were located using the climbing image-nudged elastic band method[51]. The Gibbs free energy (ΔG) for C_1–C_1 and C_1–C_2 coupling was calculated by converting the electronic energy using the equation: $\Delta G = \Delta E + \Delta ZPE + \int \Delta C_p dT - T\Delta S$, where ΔE, ΔZPE, ΔC_p, and ΔS are the differences in electronic energy, zero-point energy, heat capacity and entropy, respectively, and T is set to room temperature (298.15 K). Here DFT calculations do not explicitly consider the dynamic changes in the surface richness of Ag–Ru–Cu. The theoretical exploration of dynamic changes of the surface under catalysis will be an important aspect of future studies.

Data availability

All data are available within the paper, Supplementary Information and source data files. Source data are provided with this paper.

Received: 30 June 2021; Accepted: 7 December 2021;
Published online: 10 February 2022

References

1. Jhong, H.-R., Ma, S. & Kenis, P. J. A. Electrochemical conversion of CO_2 to useful chemicals: current status, remaining challenges, and future opportunities. *Curr. Opin. Chem. Eng.* **2**, 191–199 (2013).
2. Wu, Y., Jiang, Z., Lu, X., Liang, Y. & Wang, H. Domino electroreduction of CO_2 to methanol on a molecular catalyst. *Nature* **575**, 639–642 (2019).
3. Xia, C. et al. Continuous production of pure liquid fuel solutions via electrocatalytic CO_2 reduction using solid-electrolyte devices. *Nat. Energy* **4**, 776–785 (2019).
4. Dinh, C.-T. et al. CO_2 electroreduction to ethylene via hydroxide-mediated copper catalysis at an abrupt interface. *Science* **360**, 783–787 (2018).

5. Wang, X. et al. Efficient electrically powered CO_2-to-ethanol via suppression of deoxygenation. *Nat. Energy* **5**, 478–486 (2020).
6. Jouny, M., Luc, W. & Jiao, F. High-rate electroreduction of carbon monoxide to multi-carbon products. *Nat. Catal.* **1**, 748–755 (2018).
7. Jouny, M., Hutchings, G. S. & Jiao, F. Carbon monoxide electroreduction as an emerging platform for carbon utilization. *Nat. Catal.* **2**, 1062–1070 (2019).
8. Service, R. F. Hunt for renewable plastics clears a hurdle. *Science* **371**, 873 (2021).
9. Hauch, A. et al. Recent advances in solid oxide cell technology for electrolysis. *Science* **370**, eaba6118 (2020).
10. Küngas, R. Review—electrochemical CO_2 reduction for CO production: comparison of low- and high-temperature electrolysis technologies. *J. Electrochem. Soc.* **167**, 044508 (2020).
11. Skafte, T. L. et al. Selective high-temperature CO_2 electrolysis enabled by oxidized carbon intermediates. *Nat. Energy* **4**, 846–855 (2019).
12. Klabunde, J., Bischoff, C. & Papa, A. J. *Ullmann's Encyclopedia of Industrial Chemistry* (Wiley, 2018).
13. Jouny, M., Luc, W. & Jiao, F. General techno-economic analysis of CO_2 electrolysis systems. *Ind. Eng. Chem. Res.* **57**, 2165–2177 (2018).
14. Bushuyev, O. S. et al. What should we make with CO_2 and how can we make it? *Joule* **2**, 825–832 (2018).
15. Li, J. et al. Copper adparticle enabled selective electrosynthesis of *n*-propanol. *Nat. Commun.* **9**, 4614 (2018).
16. Zhuang, T.-T. et al. Copper nanocavities confine intermediates for efficient electrosynthesis of C_3 alcohol fuels from carbon monoxide. *Nat. Catal* **1**, 946–951 (2018).
17. Pang, Y. et al. Efficient electrocatalytic conversion of carbon monoxide to propanol using fragmented copper. *Nat. Catal.* **2**, 251–258 (2019).
18. de Arquer, F. P. G. et al. CO_2 electrolysis to multicarbon products at activities greater than 1 A cm^{-2}. *Science* **367**, 661–666 (2020).
19. Zhuang, T.-T. et al. Steering post-C-C coupling selectivity enables high efficiency electroreduction of carbon dioxide to multi-carbon alcohols. *Nat. Catal.* **1**, 421–428 (2018).
20. Jiang, K. et al. Metal ion cycling of Cu foil for selective C–C coupling in electrochemical CO_2 reduction. *Nat. Catal.* **1**, 111–119 (2018).
21. Xiao, H., Cheng, T. & Goddard, W. A. Atomistic mechanisms underlying selectivities in C_1 and C_2 products from electrochemical reduction of CO on Cu (111). *J. Am. Chem. Soc.* **139**, 130–136 (2016).
22. Kuhl, K. P., Cave, E. R., Abram, D. N. & Jaramillo, T. F. New insights into the electrochemical reduction of carbon dioxide on metallic copper surfaces. *Energy Environ. Sci.* **5**, 7050–7059 (2012).
23. Wang, X. et al. Efficient upgrading of CO to C_3 fuel using asymmetric C–C coupling active sites. *Nat. Commun.* **10**, 5186 (2019).
24. Montoya, J. H., Shi, C., Chan, K. & Nørskov, J. K. Theoretical insights into a CO dimerization mechanism in CO_2. *J. Phys. Chem. Lett.* **6**, 2032–2037 (2015).
25. Xiao, H., Goddard, W. A., Cheng, T. & Liu, Y. Cu metal embedded in oxidized matrix catalyst to promote CO_2 activation and CO dimerization for electrochemical reduction of CO_2. *Proc. Natl Acad. Sci. USA* **114**, 6685–6688 (2017).
26. Lum, Y., Cheng, T., Goddard, W. A. & Ager, J. W. Electrochemical CO reduction builds solvent water into oxygenate products. *J. Am. Chem. Soc.* **140**, 9337–9340 (2018).
27. Hussain, J., Jonsson, H. & Skulason, E. Calculations of product selectivity in electrochemical CO_2 reduction. *ACS Catal.* **8**, 5240–5249 (2018).
28. Goodpaster, J. D., Bell, A. T. & Head-Gordon, M. Identification of possible pathways for C–C bond formation during electrochemical reduction of CO_2: new theoretical insights from an improved electrochemical model. *J. Phys. Chem. Lett.* **7**, 1471–1477 (2016).
29. Cobley, C. M. & Xia, Y. Engineering the properties of metal nanostructures via galvanic replacement reactions. *Mater. Sci. Eng. R* **70**, 44–62 (2010).
30. Clark, E. L., Hahn, C., Jaramillo, T. F. & Bell, A. T. Electrochemical CO_2 reduction over compressively strained CuAg surface alloys with enhanced multi-carbon oxygenate selectivity. *J. Am. Chem. Soc.* **139**, 15848–15857 (2017).
31. Han, L., Wang, P., Liu, H., Tan, Q. & Yang, J. Balancing the galvanic replacement and reduction kinetics for the general formation of bimetallic CuM (M = Ru, Rh, Pd, Os, Ir, and Pt) hollow nanostructures. *J. Mater. Chem. A* **4**, 18354–18365 (2016).
32. Mistry, H. et al. Highly selective plasma-activated copper catalysts for carbon dioxide reduction to ethylene. *Nat. Commun.* **7**, 12123 (2016).
33. Zhou, Y. et al. Dopant-induced electron localization drives CO_2 reduction to C_2 hydrocarbons. *Nat. Chem.* **19**, 974–980 (2018).
34. Hoang, T. T. H. et al. Nanoporous copper–silver alloys by additive-controlled electrodeposition for the selective electroreduction of CO_2 to ethylene and ethanol. *J. Am. Chem. Soc.* **140**, 5791–5797 (2018).
35. Gunathunge, C. M. et al. Spectroscopic observation of reversible surface reconstruction of copper electrodes under CO_2 reduction. *J. Phys. Chem. C* **121**, 12337–12344 (2017).
36. Sheppard, N. & Nguyen, T. T. in *Advances in Infrared and Raman Spectroscopy* (eds Clark, R. J. H. & Hester, R. E.) Ch. 5 (Heyden, 1978).
37. Gunathunge, C. M., Ovalle, V. J., Li, Y., Janik, M. J. & Waegele, M. M. Existence of an electrochemically inert CO population on Cu electrodes in alkaline pH. *ACS Catal.* **8**, 7507–7516 (2018).
38. Fielicke, A., Gruene, P., Meijer, G. & Rayner, D. M. The adsorption of CO on transition metal clusters: a case study of cluster surface chemistry. *Surf. Sci.* **603**, 1427–1433 (2009).
39. Sandberg, R. B., Montoya, J. H., Chan, K. & Nørskov, J. K. CO–CO coupling on Cu facets: coverage, strain and field effects. *Surf. Sci.* **654**, 56–62 (2016).
40. Luc, W., Rosen, J. & Jiao, F. An Ir-based anode for a practical CO_2 electrolyzer. *Catal. Today* **288**, 79–84 (2017).
41. Ravel, B. & Newville, M. ATHENA, ARTEMIS, HEPHAESTUS: data analysis for X-ray absorption spectroscopy using IFEFFIT. *J. Synchrotron Radiat.* **12**, 537–541 (2005).
42. Rumble, J. R. *CRC Handbook of Chemistry and Physics* 99th edn (CRC Press, 2018).
43. Kresse, G. & Furthmüller, J. Efficient iterative schemes for ab initio total-energy calculations using a plane-wave basis set. *Phys. Rev. B* **54**, 11169–11186 (1996).
44. Kresse, G. & Furthmuller, J. Efficiency of ab-initio total energy calculations for metals and semiconductors using a plane-wave basis set. *Comp. Mater. Sci.* **6**, 15–50 (1996).
45. Kresse, G. & Hafner, J. Ab initio molecular-dynamics simulation of the liquid-metal amorphous-semiconductor transition in germanium. *Phys. Rev. B* **49**, 14251–14269 (1994).
46. Kresse, G. & Hafner, J. Ab initio molecular dynamics for liquid metals. *Phys. Rev. B* **47**, 558–561 (1993).
47. Perdew, J. P., Burke, K. & Ernzerhof, M. Generalized gradient approximation made simple. *Phys. Rev. Lett.* **77**, 3865–3868 (1996).
48. Monkhorst, H. J. & Pack, J. D. Special points for Brillouin-zone integrations. *Phys. Rev. B* **13**, 5188–5192 (1976).
49. Grimme, S., Antony, J., Ehrlich, S. & Krieg, H. A consistent and accurate ab initio parametrization of density functional dispersion correction (DFT-D) for the 94 elements H–Pu. *J. Chem. Phys.* **132**, 154104 (2010).
50. Montoya, J. H., Shi, C., Chan, K. & Nørskov, J. K. Theoretical insights into a CO dimerization mechanism in CO_2 electroreduction. *J. Phys. Chem. Lett.* **6**, 2032–2037 (2015).
51. Henkelman, G., Uberuaga, B. P. & Jónsson, H. A climbing image nudged elastic band method for finding saddle points and minimum energy paths. *J. Chem. Phys.* **113**, 9901–9904 (2000).

Acknowledgements

This work was supported by the Natural Sciences and Engineering Research Council (NSERC) of Canada (number RGPIN-2017-06477, E.H.S.) and the Ontario Research Fund—Research Excellence Program (number ORF-RE08-034, E.H.S.). DFT calculations were performed on the Niagara supercomputer at the SciNet HPC Consortium. We acknowledge the computational resources supported by SciNet, which is funded by the University of Toronto, the Ontario Research Fund—Research Excellence Program, the Government of Ontario and the Canada Foundation for Innovation. D.S. acknowledges the NSERC E.W.R. Steacie Memorial Fellowship. Synchrotron measurements were carried out at the BL-17C at the National Synchrotron Radiation Research Center. We thank R. Wolowiec and D. Kopilovic for their kind technical assistance, Ontario Centre for the Characterization of Advanced Materials (OCCAM) of the University of Toronto and the National Synchrotron Radiation Research Center.

Author contributions

E.H.S. supervised the project. X.W. and E.H.S. conceived the idea. X.W. designed and carried out the experiments. P.O. carried out DFT calculations. S.-F.H. performed XAS measurements. S.-F.H. and J.A. analysed the XAS data. A.O. fabricated the IrO_x-coated Ti mesh electrodes. J.T. and J.Y.H. contributed to the SEM and TEM characterization. X.W and J.S. did the TEA. K.B. and ASR carried out XPS measurements. X.W. and M.S. performed XRD measurements. C.M.G. and F.P.G.d.A. contributed to the manuscript editing. X.W., P.O., and E.H.S. co-wrote the manuscript. R.K.M., C.P.O, Z.W., A.H.I. and D.S. assisted with the discussions. All authors discussed the results and assisted during manuscript preparation.

Competing interests

X.W. and E.H.S. have filed a provisional patent application titled 'Manufacturing and use of co-doped multi-metallic electrocatalysts for upgrading of CO to propanol' (application number 63/192,842). All other authors declare no competing interests.

Additional information

Supplementary information The online version contains supplementary material available at https://doi.org/10.1038/s41560-021-00967-7.

Correspondence and requests for materials should be addressed to Edward H. Sargent.

Peer review information *Nature Energy* thanks Maximilian Fleischer, Xiaowa Nie and the other, anonymous, reviewer(s) for their contribution to the peer review of this work.

Reprints and permissions information is available at www.nature.com/reprints.

Publisher's note Springer Nature remains neutral with regard to jurisdictional claims in published maps and institutional affiliations.